medRxiv preprint doi: https://doi.org/10.1101/2023.04.14.23288516; this version posted April 17, 2023. The copyright holder for this preprint (which was not certified by peer review) is the author/funder, who has granted medRxiv a license to display the preprint in perpetuity. It is made available under a CC-BY-NC-ND 4.0 International license .

Multimodal imaging of microstructural cerebral changes and loss of synaptic density in Alzheimer's disease

Soodeh Moallemian, Eric Salmon, Mohamed Ali Bahri, Nikita Beliy, Emma Delhaye, Evelyne Balteau, Christian Degueldre, Christophe Phillips[*a], Christine Bastin[*a]

GIGA-Cyclotron Research Centre-in vivo imaging, University of Liège, Allée du 6 Août, 8, Liège, B30, 4000, Belgium

Abstract

Multiple neuropathological changes are involved in Alzheimer's disease (AD). AD hallmark biomarkers are amyloid-beta, tau pathology, and neuronal and synaptic loss. Other possible brain tissue-related biomarkers, such as iron and myelin content in the brain, are less frequently studied. Thanks to quantitative MRI (qMRI), tissue parameters such as magnetization transfer (MT), effective transverse relaxation (R2*), and proton density (PD) can be determined quantitatively, enabling the detection of microstructural tissue-related alterations in aging and neurodegenerative diseases. The current study investigated the co-occurrence of neurodegeneration (as measured with synaptic density), increased iron content, and decreased myelin content in Alzheimer's disease. The study involved 24 amyloid-positive patients (AD, 11 males) and 19 healthy controls (HC, 9 males). All participants underwent a multi-parameter mapping MRI protocol, from which quantitative maps for MTsat and R2* were estimated. Synaptic density was indexed by the total volume distribution map (Vt) derived from [18F] UCB-H PET imaging. First, groups were compared with univariate statistical analyses applied to R2*, MTsat and Vt maps. Then multivariate General Linear Model (mGLM) was used to detect the co-occurrence of changes in R2*, MTsat, and Vt at the voxel level. Univariate GLM analysis of R2* showed no significant difference between the two groups. In contrast, the same analysis for MTsat resulted in a significant between-group difference in the right hippocampus at the cluster level with a corrected threshold (P-value < .05). The mGLM analysis revealed a significant difference in both right and left hippocampus between the AD and HC groups, as well as in the left precuneus, right middle frontal, and left superior orbitofrontal gyrus when all three modalities were present, suggesting these regions as the most affected despite the diverse changes of myelin, iron, and synapse degeneration in AD. Here, the mGLM is introduced as an alternative for multiple comparisons between different modalities, as it reduces the risk of false positives due to the multiplicity of the tests while informing about the co-occurrence of neuropathological processes in dementia.

Keywords: Alzheimer's disease, qMRI, PET, Multivariate analysis

* Corresponding author.

[a] *Contributed equally*

Email addresses: c.phillips@uliege.be (Christophe Phillips), christine.bastin@uliege.be (Christine Bastin)

NOTE: This preprint reports new research that has not been certified by peer review and should not be used to guide clinical practice.

medRxiv preprint doi: https://doi.org/10.1101/2023.04.14.23288516; this version posted April 17, 2023. The copyright holder for this preprint (which was not certified by peer review) is the author/funder, who has granted medRxiv a license to display the preprint in perpetuity. It is made available under a CC-BY-NC-ND 4.0 International license .

1 Introduction

Concomitantly with an increase in average life expectancy, a major epidemiologic trend of the current century is the rise of neurodegenerative diseases worldwide, among which Alzheimer's disease (AD) is the most common type, with 60 to 80 percent of the cases (Calabrò et al., 2021). Despite an incipient decrease in incidence, notably because of the prevention of vascular diseases in western countries, AD prevalence is expected to rise because this neurodegenerative disease increases exponentially with age (Azam et al., 2021; C.-C Tan, 2014). It is recognized that AD pathological processes unfold decades before the emergence of clinical signs of cognitive decline (Dean et al., 2017; Gonneaud and Chételat, 2018; Tan et al., 2014). These pathological processes include a progressive accumulation of amyloid-beta plaques and tau neurofibrillary tangles (NFT), in addition to synaptic and neuronal loss (Gulisano et al., 2018; Jack et al., 2013; Spillantini and Goedert, 2013; Tan et al., 2014; Yin et al., 2021). According to the amyloid cascade hypothesis (Jack et al., 2013), amyloid plaques are the initial cause of AD, triggering tau NFT, synaptic and neuronal loss. However, this view has changed notably with the constant development of novel imaging tools (Calabrò et al., 2021; Yin et al., 2021). For instance, tau NFT seems to collocate much more with synaptic and neuronal loss than amyloid neuritic plaques. Likewise, once AD cognitive symptoms are detected, tau NFT burden follows cognitive decline more closely than amyloid plaques (Musiek and Holtzman, 2015). Besides tau pathology, synaptic loss appears as the best correlate of cognitive decline in patients with Mild Cognitive Impairment (MCI) and with AD (DeKosky and Scheff, 1990; Scheff et al., 2006; Terry et al., 1991). Also, in about 40% of cognitively normal older individuals, neurodegeneration (hippocampal atrophy) precedes detection of amyloid plaques (Jeremic et al., 2021; Villemagne et al., 2011). However, amyloid plaques might be required for tau NFT to expand from subcortical to cortical areas. Therefore, the relationships between AD hallmarks are more complex than first apprehended and could arise (partly) from relatively independent phenomena converging to AD. Accordingly, the identification of the early events in the AD pathophysiological cascade with in vivo noninvasive methods is critical to increase our understanding of the disease and inform the search for a treatment.

In the quest for early biomarkers, it has been suggested that changes in brain microstructure are among the first manifestations of AD (Bartzokis, 2011). Increased iron levels are associated with dysfunction of oligodendrocytes, notably impacting myelin repair. Moreover, an increase in free iron is toxic, inducing oxidative stress and inflammation, cell dysfunction, and, ultimately, cell death (Bartzokis, 2011; Bulk et al., 2018; Calabrò et al., 2021). So, it is hypothesized that myelin breakdown and increases in iron levels are very early events in the physiopathology of Alzheimer's disease. In support of this "myelin and iron" hypothesis, histological studies showed that myelin breakdown in early AD occurs mainly in frontal and temporoparietal areas (Bartzokis, 2011; Bulk et al., 2018; Kalpouzos et al., 2017; Zecca et al., 2004). Increased iron content was also found in frontal and temporal areas of AD patients (Bulk et al., 2018; House et al., 2008). Moreover *ex-vivo* studies showed that altered iron accumulation is positively correlated with the number of amyloid-beta plaques in these areas (Duijn, 2017; van Bergen et al., 2016). Elevated iron content has also been observed in the hippocampus of AD patients (Zeineh et al., 2015). Additionally, higher levels of ferritin (i.e., the principal iron storage protein of the body) in the cerebrospinal fluid (CSF) are associated with the poorer cognitive performance of cognitively normal, MCI and AD participants, and predicted MCI conversion to AD (Ayton et al., 2015; Peng et al., 2021).

Novel neuroimaging tools can be used to assess brain microstructure. Indeed, specific MRI parameters have differential sensitivity for structural aspects of tissue such as fiber coherence, macromolecules, myelin, iron, and water content. Recently developed quantitative MRI techniques offer, through their

medRxiv preprint doi: https://doi.org/10.1101/2023.04.14.23288516; this version posted April 17, 2023. The copyright holder for this preprint (which was not certified by peer review) is the author/funder, who has granted medRxiv a license to display the preprint in perpetuity. It is made available under a CC-BY-NC-ND 4.0 International license .

sensitivity to microstructural tissue properties, a unique opportunity for establishing in vivo the link to findings of postmortem histological assessment of brain tissue. Notably, Multi-Parameter Mapping (MPM) has been used to create quantitative brain maps that lead to a highly specific inference of tissue properties such as myelin water fraction (i.e., myelination) and iron content in the gray matter (Draganski et al., 2011). Consistently with *ex-vivo* histological studies indicating degeneration of myelin sheaths with healthy aging (Peters, 2002), myelin water fraction as measured by MPM magnetization transfer saturation maps (MTsat) was found to decrease with aging in the corpus callosum as well as in frontal and parietal white matter (Callaghan et al., 2014). Additionally, in line with *ex-vivo* evidence of increased iron content in basal ganglia in normal aging (Bulk et al., 2018), MPM imaging detected in vivo a positive correlation between iron deposit in the basal ganglia and age (Callaghan et al., 2014; Draganski et al., 2011). Increased iron content was related to lower blood oxygen level dependent (BOLD) signal in older adults (Kalpouzos et al., 2017).

In this context, our main objective was to use quantitative MRI to detect in vivo microstructural changes (myelin water fraction and iron content) in individuals with AD diagnosed by significant amyloid burden in the brain by comparison to healthy older individuals (amyloid-negative and cognitively healthy). In AD, investigation of brain microstructure with quantitative MRI has only recently started. One study (Acosta-Cabronero et al., 2016) used quantitative susceptibility mapping in MRI to show that AD patients have increased iron content in the putamen, caudate nucleus, and amygdala. The same authors (Acosta-Cabronero et al., 2013) indicated that in healthy older adults, iron accumulation can be found in frontal lobes, affecting brain regions related to motor functions. Steiger and colleagues observed a decrease in gray matter volume and myelin, and an increase of iron in widespread brain regions including the basal ganglia in older adults using quantitative MRI technique (Steiger et al., 2016). Another work directly evaluated, in healthy older participants, the concurrent relation between CSF markers of amyloid-beta and tau AD pathology, and MRI relaxometry-based measures of myelin content in the brain (Dean et al., 2017). They found that lower CSF amyloid-beta and higher tau levels were related to regional decreases in the brain MRI myelin measures, particularly in brain regions known to be preferentially affected in AD, including white matter in the frontal, temporal, corpus callosum, and cingulum regions.

To our knowledge, no study has used quantitative MPM to assess *in-vivo* myelin and iron in AD concomitantly. Moreover, little is known about *in-vivo* co-occurrence of cerebral microstructural changes and synaptic loss. The latter can be assessed with PET imaging using radiotracers binding to synaptic vesicle protein 2A (SV2A). With SV2A-PET imaging, AD-related decreased synaptic density was found in several cortical areas and the thalamus, with the most significant effect size in the hippocampus (Bastin et al., 2020; Chen et al., 2018).

In the current study, co-occurrence of microstructural changes with reduced regional cerebral uptake of [18F]UCB-H PET indexing synaptic density was assessed with a multivariate model applied to the different imaging modalities (MPM and SV2A-PET). If myelin decrease and iron burden are early events preceding synaptic loss and neuronal death (Bartzokis, 2011), one should observe a co-occurrence in microstructural changes and decreased synaptic density, likely in the hippocampus whose alteration drives symptoms in the patients (Bastin et al., 2020). Of note, in the current cross-sectional study, we cannot assess the chronology of pathological changes across the different modalities. Nevertheless, we hypothesize that, if pathological processes are triggering one another as suggested by Bartzokis (2011), one should observe co-localization of pathological changes in the brain.

medRxiv preprint doi: https://doi.org/10.1101/2023.04.14.23288516; this version posted April 17, 2023. The copyright holder for this preprint (which was not certified by peer review) is the author/funder, who has granted medRxiv a license to display the preprint in perpetuity. It is made available under a CC-BY-NC-ND 4.0 International license .

2 Methods

2.1 Participants

The data come from a published study that focused on in-vivo imaging of synaptic loss (Bastin et al., 2020). Two groups of older participants were included in the study. The first group consisted of 24 amyloid-positive patients from the AD continuum (Aβ-positive group). These patients were recruited from the Memory Clinic at Liege University Hospital. They were diagnosed based on current NIA-AA criteria (Albert et al., 2011; Jack et al., 2018; McKhann et al., 2011). As part of the initial diagnostic process, [18F]FDG-PET was used as a biomarker of neurodegeneration in all patients. Also, global cognition was assessed with the Mini-mental state examination (MMSE). Aβ positivity was determined based on [18F]Flutemetamol-PET by qualitative visual inspection and by cortical standardized uptake value ratios (SUVR) above a quantitative threshold determined in a database of healthy older adults (Bastin et al., 2020). In Aβ-positive group, 6 patients were diagnosed with MCI (MMSE between 26 and 30) and 19 with probable AD, with MMSE scores between 14 and 26 (mild stage, MMSE > 20, n = 15; moderate stage, MMSE< 20, n = 4). The second group comprised 19 cognitively healthy controls (HC) (with MMSE between 28 and 30). In the HC group, amyloid-negativity was confirmed in eight participants, while there was no biomarker-related information for the others. Both groups were matched for age, sex, and education.

2.2 Data acquisition

Our data consists of dynamic PET and MRI.

2.2.1 SV2A-PET

Dynamic PET acquisitions were carried out using a Siemens/ CTI (Knoxville, TN) ECAT HR+ PET scanner. An intravenous bolus of [18F]UCB-H[37] of 157.06 8.96 MBq was administered. For a total of 100 minutes, the dynamic PET was conducted with time frames of 6*10s, 8*30s, 5*120s, and 17*300s. All PET images were reconstructed using filtered back projection (Hann filter, 4.9 mm FWHM), including corrections for measured attenuation, dead time, random events, and scatter using standard software (ECAT 7.1, Siemens/CTI, Knoxville, TN). The transaxial resolution in water, under these acquisition and reconstruction conditions, is 6.5–7 mm (voxel size 2.57 x 2.57 x 2.43 mm^3). A mean unchanged plasma fraction was calculated for each group and used for modeling based on blood samples collected in 7 controls and 6 patients. Further information on PET acquisition and processing can be found in (Bastin et al., 2020).

2.2.2 Multi-Parametric Mapping quantitative MRI

MRI data has been acquired on a 3T whole-body MRI-scanner (Magnetom Prisma, Siemens Medical Solution, Erlangen, Germany) using a standard 32-channel head receiving coil. The whole-brain MRI acquisitions included a multiparameter mapping protocol (MPM) (Weiskopf et al., 2013), from which (semi)quantitative maps of magnetization transfer saturation (MTsat), proton density (PD), transverse relaxation (R1), and effective longitudinal relation (R2*) can be estimated. This protocol consists of 3 co-localized 3D multi-echo fast low angle shot (FLASH) acquisitions with 1 mm isotropic resolution and 2 additional calibration sequences to correct for inhomogeneities in the RF transmit field (Lutti et al., 2010). The FLASH datasets were acquired with predominantly PD, T1 and MT weighting determined by the repetition time and flip angle, referred to in the following as PDw, T1w and MTw echoes. MTw contrast was obtained using an additional off-resonance Gaussian-shaped RF pulse. All three had high bandwidth to minimize off-resonance and chemical shift artifacts. Volumes were acquired in 176 sagittal slices using a 256x224 voxel matrix. GRAPPA parallel imaging was combined with partial Fourier acquisition to

medRxiv preprint doi: https://doi.org/10.1101/2023.04.14.23288516; this version posted April 17, 2023. The copyright holder for this preprint (which was not certified by peer review) is the author/funder, who has granted medRxiv a license to display the preprint in perpetuity. It is made available under a CC-BY-NC-ND 4.0 International license .

speed up acquisition time to approximately 20 min. B1 field mapping images (transmit B1+ and receive B1- fields) were also acquired to reduce spatial heterogeneities related to B1 effect, which was essential for proper quantification of T1 (or R1=1/T1) in particular. Finally, B0 field mapping images were acquired for image distortions correction: two magnitude images acquired at 2 different TE's, and pre-subtracted phase images.

2.3 Image data processing

Collected data were anonymized and organized according to the Brain Imaging Data Structure (BIDS) (Gorgolewski et al., 2016) and its extensions for PET (Knudsen et al., 2020) and qMRI (Karakuzu et al., 2022) data, the latter using BIDSme (https://github.com/CyclotronResearchCentre/bidsme), and the former with custom MATLAB scripts. All information needed for subsequent analysis was incorporated into the dataset. Data is available from the corresponding authors upon reasonable request.

2.3.1 MRI

To obtain the quantitative maps, MRI data were processed with SPM12 (www.fil.ion.ucl.ac.uk/spm) and the hMRI (https://hmri.info/) toolbox, where the latter is an extension to SPM (Tabelow et al., 2019). T1w, PDw, and MTw images acquired at multiple TEs were extrapolated to TE=0 to increase the signal-to-noise ratio and remove the otherwise remaining R2* bias (Tabelow, 2019). The TE=0 extrapolated MTw, PDw, and T1w images were used to calculate MT saturation, R1 and apparent signal amplitude A* maps. A* maps were rescaled to generate PD maps. All quantitative maps were corrected for inhomogeneities from local RF transmit field (B1+). The receive bias field map (B1-) was used to correct PD maps for instrumental biases (Ashburner and Friston, 2005). R2* maps were estimated using the ESTATICS method from the three different FLASH acquisitions by accounting for the varying contrasts. The ordinary least squares (OLS) log-linear fit was also used to detect and down weight echoes affected by motion artifacts (Weiskopf et al., 2014). R1 maps were corrected for the radio frequency (RF) transmit field inhomogeneity B1+ (Preibisch and Deichmann, 2009). Quantitative maps were segmented into gray matter (GM), white matter (WM), and cerebrospinal fluid (CSF) using the unified segmentation approach as implemented in SPM (Ashburner and Friston, 2005). Inter-subject registration of the GM and WM tissue maps was performed using DARTEL, a nonlinear diffeomorphic algorithm (Ashburner, 2007). This algorithm estimates the deformations that best align the tissue probability maps by iterative registration of these maps to their average. The tissue probability maps were then normalized to the stereotactic space specified by the Montreal Neurological Institute (MNI) template using the resultant DARTEL template and deformations. Then, specific tissue-weighted smoothing, with a 3mm FWHM isotropic kernel, was applied to avoid mixing values from different tissues classes, as would happen with standard Gaussian smoothing.

A GM mask was created using the mean segmented MTsat image from all subjects to be later used as an explicit mask in the statistical analysis.

2.3.2 PET

PET data were processed as described previously (Bastin et al., 2020). In brief, [18F]UCB-H PET dynamic frames were corrected for motion without re-slicing. The images were corrected for partial volume effects (PVE) using the iterative Yang voxel-wise method implemented in the PETPVC toolbox (Thomas et al., 2016), with GM, WM, CSF and "other" as ROI masks. Kinetic modeling using PVE-corrected dynamic PET data and image-derived input function was done with PMOD (Version 3.7, PMOD Technologies, Zurich, Switzerland). Input function was derived from the dynamic images (Bahri et al., 2017) and corrected for metabolites using the measured group mean unchanged plasma fraction. Logan graphical analysis (with t* = 25 min) was used to calculate the distribution volume (Vt) map of

medRxiv preprint doi: https://doi.org/10.1101/2023.04.14.23288516; this version posted April 17, 2023. The copyright holder for this preprint (which was not certified by peer review) is the author/funder, who has granted medRxiv a license to display the preprint in perpetuity. It is made available under a CC-BY-NC-ND 4.0 International license .

[18F]UCB-H in the brain. Finally individual Vt maps were coregistered with their corresponding MTsat map, then their spatial normalization transformations were applied to warp the Vt maps in the same reference space.

2.4 Statistical analyses

All analyses focused on GM only as PET images indexing synaptic density are only interpretable for gray matter. Therefore, an explicit mask for GM was applied on all the analysis. Since each parametric map has a specific unit, e.g., Hertz for R2* images and ml/cm3 for Vt maps, their intensities are not directly comparable. Thus, all maps were Z-transformed - per modality and across subjects - using the grand mean and variance over each voxel, to ensure comparability of different modalities for our multivariate analysis. All statistical analyses were performed on the standardized data.

For quantitative MRI, we decided not to investigate R1 and PD maps, as they are proportional to multiple tissue properties at the same time, and would lead to underestimation of microstructural changes that we are interested in. Three modalities (MTsat, R2*, and Vt) were individually analyzed using a univariate 2-sample t-test GLM with age and sex of the participants as covariates. We tested for the difference between the two groups for each modality. The t-student contrast defined for MTsat maps was HC>AD, hypothesizing that healthy controls have more myelin than AD patients, considering MTsat maps are proportional to the level of myelin in the brain. For R2* maps, we used contrasted AD>HC, testing hypothesizing that R2* values in AD group are superior to those of healthy subjects, as increased iron load is considered toxic. For Vt maps, we also tested the difference between groups (HC>AD).

A MANOVA model was specified using the design matrixes of the three univariate models in the MSPM toolbox (Gyger et al., 2021), a newly developed toolbox working under SPM as a multivariate extension of univariate GLM (Chen et al., 2014; M Mcfarquhar, 2016). The multivariate GLM (mGLM) models the multivariate observations as Y=XB+E, where $Y_{43\times3}=[Y_1,Y_2,Y_3]$ is the multi-modal data matrix, each row of Y represents one subject, and each column of Y represents one modality MTsat, R2*, and Vt at a single voxel; and $X_{43\times4}=[X_1,X_2,X_3,X_4]$is the design matrix, representing the AD and HC groups in the first two columns, and age and sex of the participants in the last two columns. The matrix B is a 4 × 3 matrix of size of regression coefficients; and E is the residual matrix of size 43 × 3. $X_{43\times4}=[X_1,X_2,X_3,X_4]$. The matrix *B* is estimated using an ordinary least-square method: $\hat{B}=(X^TX)^{-1}X^TY$, the matrix of predicted response value is $\hat{Y}=X\hat{B}$, and the residual matrix is $E=Y-\hat{Y}$.

The regression model can be used to partition the total variation in the outcome into explained variance and unexplained variance. In this sense, the total sums of square and cross products (SSCP) terms are calculated as: $SSCP_{Total}=SSCP_{Model}+SSCP_{Residual}$. The SSCP matrix is used to estimate the variance-covariance matrix of the predictor variables in linear regression analysis, and can be presented as $SSCP_{Total}=(\hat{Y}^T\hat{Y}-N\bar{y}\bar{y}^T)+E^TE$, where N=3 , the total number of observations. To test the null hypothesis that all the coefficients in B are equal to zero, we can compute the eigenvalues of $SSCP_{Model}SSCP^{-1}_{Residual}$. Therefore, we must solve (Eq. 1) for finding the q eigenvalues λ and corresponding eigenvectors:

$$\det\left(\frac{\hat{Y}^T\hat{Y}-N\bar{y}\bar{y}^T}{E^TE}-\lambda I_q\right)=0 \qquad (1)$$

Then the Wilk's lambda summary statistics Λ is calculated based on the eigenvalues solving the equation of eigen-decomposition for the determinant matrix as follow:

medRxiv preprint doi: https://doi.org/10.1101/2023.04.14.23288516; this version posted April 17, 2023. The copyright holder for this preprint (which was not certified by peer review) is the author/funder, who has granted medRxiv a license to display the preprint in perpetuity. It is made available under a CC-BY-NC-ND 4.0 International license .

$$\Lambda = \frac{|SSCP_{Model}|}{|SSCP_{Model}+SSCP_{Residual}|} = \prod_{i=1}^{q} \frac{1}{1+\lambda_i} \tag{2}$$

To test the hypothesis of the association between all dependent variables and contrasts among predictors, we applied this linear hypothesis: $H_0: CBL = 0$, where $L_{3\times3}$ is a full rank matrix to test the hypothesis, here an identity matrix to test the hypothesis for the joint effect of all modalities (columns of B). The contrast matrix $C=[1,-1,0,0]$ would perform a standard F-test to assess the difference between the 2 groups, AD and HC. Then, SS matrices associated with the hypothesis are calculated as follows:

$$SSCP_{Hyp} = \left(C\hat{B}L\right)^T \left(C\hat{B}L\right) \tag{3}$$

$$SSCP_{Residual} = L\left(\hat{E}^T\hat{E}\right)L^T \tag{4}$$

Then the Wilk's lambda summary statistics Λ is calculated by (Eq. 2). As there were three dependent variables in our model, it is interesting to extract the contribution of each modality (dependent variables) to the test statistics Λ, called canonical vector. This contribution corresponds to the eigenvectors of $SSCP_{Model}SSCP^{-1}_{Residual}$ and can be calculated by solving (Eq. 1) for each eigenvalue, see (Tabachnick and Fidell, 2007) for mathematical details.

Due to the lack of directionality in F-Tests, we are not able to interpret the results of the canonical vectors. Therefore, for illustrative purposes only, we extracted the original values, before the z-score transformation, from the 3 maps used at the voxels within significant cluster. This sheds light on the difference in real tissue property values.

Statistical inference will be performed in the Results section using a p-value < .05 "family-wise error rate" (FWER) corrected, at the voxel or cluster extent levels. For the latter, the cluster forming threshold used will be a voxel level p<.001 uncorrected.

3 Results

3.1. Univariate analyses

Controlling for age and sex, the two-sample t-test on MTsat maps revealed a significant difference at cluster-level (P_{FWE}<.05) between AD patients and healthy controls which covers the right hippocampus and amygdala indicating lower values in AD than in controls (Figure 1-B). No significant difference in R2* maps, representative of iron level content in the brain, was detected between the groups. However, it is worth mentioning that, at a more lenient statistical threshold (p < .001 uncorrected), the results for R2* analysis show differences bilaterally in the superior part of orbitofrontal cortex as well as in the left hippocampus and right mid-temporal gyrus.

Vt data shows higher intensities in healthy controls compared to Alzheimer's patients in the left and right hippocampus and amygdala at voxel-level (P_{FWE} <.05) as well as left posterior and anterior insula, right and left thalamus, and middle cingulate gyrus at cluster level (Figure 1-A). Coordinates and anatomical labels of the peaks are presented in Table1.

3.2. Multivariate analysis

medRxiv preprint doi: https://doi.org/10.1101/2023.04.14.23288516; this version posted April 17, 2023. The copyright holder for this preprint (which was not certified by peer review) is the author/funder, who has granted medRxiv a license to display the preprint in perpetuity. It is made available under a CC-BY-NC-ND 4.0 International license .

The multivariate GLM (mGLM) model, controlling for the effect of age and sex, shows significant difference at voxel-level (P_{FWE} <.05) between the two groups in both left and right hippocampus and amygdala. Differences were also observed in the right middle frontal gyrus and left inferior parietal cortex as well as the right orbitofrontal cortex (Figure 2). Coordinates and anatomical labels of the peaks are presented in Table 2.

Canonical vectors are evaluated for the mGLM model for each modality. The canonical vectors at the peak voxel of the above-mentioned clusters are illustrated in Figure 3. Currently, it is not possible to summarize and evaluate whether the profile of canonical vectors within a particular cluster is uniform or diverse. Furthermore, the interpretation of the findings is limited due to the lack of directionality of effects based on F-tests.

The violin plots in Figure 2 represent the distribution of values within the five significant clusters from the mGLM model in the original quantitative maps (before Z-transformation and after correcting for age and sex) to illustrate that the difference we detected, using the mGLM, is genuinely derived from which tissue property in each cluster. This measure of contribution reveals visually the rate of contribution of each modality within the multivariate model.

The multivariate approach results for the difference in the right hippocampus concur with those of the univariate analyses of MTsat and Vt maps. Other regions in the frontal and parietal cortex appeared to show combine alteration in AD patients in the mGLM approach but were not observed in the univariate analyses. This suggests that using the mGLM we can increase the sensitivity by performing only one test instead of multiple univariate tests.

4 Discussion

In this study, we investigated the association of synaptic density, myelination, and iron accumulation in patients with Alzheimer's disease (i.e., presence of cerebral amyloid burden) compared to healthy individuals. The three different markers are assumed to play a role during AD, with a hypothesized cascade of pathological processes whereby increased iron and decreased myelin would lead to neuronal death and a reduction of synapses (Bartzokis, 2011). Only a longitudinal study could capture this hypothetical chronology. Nevertheless, we hypothesized that, when reaching the clinical stage where amyloid-positive individuals demonstrate symptoms of cognitive decline, co-occurrence of changes in the three pathological markers should be seen if they were linked in previous stages. Although the current study is based on a small sample of participants, the findings suggest that combining different image-derived AD risk factors in a multimodal analysis cohort allowed us to identify specific regions of the brain harboring a co-occurrence of several neuropathological processes involved in the early stage of AD.

The univariate comparison of AD patients and controls for each microstructural cerebral map already provides complementary findings to the scarce data assessing *in-vivo* Alzheimer-related changes in iron burden and myelination. Although myelin is continuously generated throughout life (Chen, 2021; Nasrabady et al., 2018), as we age, myelin generation decreases which affects cognitive functioning (Wang et al., 2020, 2018). Myelin deficits are shown to cause neurological setbacks such as motor dysfunction and neural degeneration (Wang et al., 2018). Furthermore, demyelination is shown to be associated with higher levels of amyloid beta (Bartzokis et al., 2007; Nasrabady et al., 2018). Bartzokis et al showed that amyloid beta positivity is negatively correlated with myelination while positively associated with iron content in the brain (Bartzokis et al., 2007). Su et al. reported that the iron content in the brain increased in one year compared to the baseline in AD participants and that iron accumulation was correlated with the neuropsychiatric behavior of participants (Su et al., 2016). More generally, little is

medRxiv preprint doi: https://doi.org/10.1101/2023.04.14.23288516; this version posted April 17, 2023. The copyright holder for this preprint (which was not certified by peer review) is the author/funder, who has granted medRxiv a license to display the preprint in perpetuity. It is made available under a CC-BY-NC-ND 4.0 International license .

known about the GM myelination in the brain (Timmler and Simons, 2019). This is the first study to investigate myelination in GM using quantitative MRI method in Alzheimer's disease. Our analysis on the MTsat maps indicates lower myelination values in the right hippocampus of the amyloid-positive patients compared to healthy controls. These results agree with the previous findings on myelin deficits that lead to motor dysfunction, impaired cognitive functions, psychiatric disorders, and neurodegenerative disease (Chen, 2021; Wang et al., 2018).

Previous in-vivo studies (Duijn, 2017; Zeineh et al., 2015) showed that although iron content in the brain is not affected by normal aging, in case of AD, accumulation of iron is observed in plaques, activated microglia, and, in the most severe cases of AD, in the mid-cortical layers along myelinated fibers. Duijn et al also showed a difference in iron and myelin distribution in frontal cortex between the healthy controls and AD patients that are visible after development of AD pathological hallmarks (Duijn, 2017). Moreover, (van Bergen et al., 2016) showed that cerebral iron is significantly positively associated with Aβ positivity in MCI. Here we failed to observe any significant group difference at the corrected statistical threshold for R2* maps indicative of iron content. However, at a more lenient statistical threshold, regions showing increased iron content correspond to those described in previous studies.

The most important findings are provided by the multivariate results indicating that there is a significant co-occurrence of demyelination, synaptic loss, and iron accumulation, in the hippocampal area bilaterally, frontal, and parietal regions of AD brains compared to healthy brains. Assuming that the probability maps are independent, the canonical vector information on the contribution of each factor shows that synaptic density and myelination contribute the most in the mGLM, while R2* maps contribute the least in all clusters (see Figure 3). The fact that co-occurrence of demyelination, iron accumulation and decreased synaptic density was found in the hippocampus may point to the determinant contribution of pathology to this region for the symptomatology from the early clinical stages of AD. Indeed, the emergence of symptoms, which concern memory in the typical form of AD, is related to neurodegeneration in the medial temporal lobe, against the background of amyloid pathology that reaches a plateau in the early stages of AD (Timmers et al., 2019). Amyloid burden in itself would not induce any cognitive decline, but its combination with neurodegeneration is the precipitating factor for the occurrence of cognitive and functional symptoms (Timmers et al., 2019). Additionally, neurodegeneration of frontal and parietal areas is also responsible for cognitive decline in early AD (Salmon et al., 2008; Yang et al., 2012). The current data may indicate that neurodegeneration is not an isolated determinant of symptoms onset.

From a methodological point of view, the multivariate analysis approach should be preferred over the use of several, one per modality studied, comparisons as it limits the implicit risk of false positive due to the multiplicity of tests with the multiple GLMs tests.

In addition to considering iron content and myelin using quantitative MRI, the novelty of the current study lies in the whole-brain assessment of combined changes in biomarkers of AD. However, there is still the need to acquire a larger dataset in which we can verify the microstructural changes of the brain through time from healthy controls to the different stages of AD, and whether they are chronologically associated with synaptic loss. More generally, the current study illustrates the importance of studying AD via its different pathological factors, as it is believed that there is a cascade of processes that lead to AD. Moreover, if we can characterize AD using non-invasive imaging techniques, we would have the opportunity to detect and study this disease in earlier stages where interventions should be the most effective.

medRxiv preprint doi: https://doi.org/10.1101/2023.04.14.23288516; this version posted April 17, 2023. The copyright holder for this preprint (which was not certified by peer review) is the author/funder, who has granted medRxiv a license to display the preprint in perpetuity. It is made available under a CC-BY-NC-ND 4.0 International license .

Acknowledgements

Funding: This work was supported by the ULiege Research Concerted Action (SLEEPDEM, grant 17/2109) and Walloon Region. [18F]flutemetamol was provided by GE Healthcare. CB is a Senior Research Associate at the F.R.S.-FNRS and CP is a Research Director at the F.R.S.-FNRS.

medRxiv preprint doi: https://doi.org/10.1101/2023.04.14.23288516; this version posted April 17, 2023. The copyright holder for this preprint (which was not certified by peer review) is the author/funder, who has granted medRxiv a license to display the preprint in perpetuity. It is made available under a CC-BY-NC-ND 4.0 International license .

Disclosure

The authors have no conflict of interest to declare.

medRxiv preprint doi: https://doi.org/10.1101/2023.04.14.23288516; this version posted April 17, 2023. The copyright holder for this preprint (which was not certified by peer review) is the author/funder, who has granted medRxiv a license to display the preprint in perpetuity. It is made available under a CC-BY-NC-ND 4.0 International license .

References

Acosta-Cabronero, J., Betts, M.J., Cardenas-Blanco, A., Yang, S., Nestor, P.J., 2016. *In Vivo* MRI Mapping of Brain Iron Deposition across the Adult Lifespan. J. Neurosci. 36, 364–374. https://doi.org/10.1523/JNEUROSCI.1907-15.2016

Acosta-Cabronero, J., Williams, G.B., Cardenas-Blanco, A., Arnold, R.J., Lupson, V., Nestor, P.J., 2013. In Vivo Quantitative Susceptibility Mapping (QSM) in Alzheimer's Disease. PLoS ONE 8, e81093. https://doi.org/10.1371/journal.pone.0081093

Albert, M.S., DeKosky, S.T., Dickson, D., Dubois, B., Feldman, H.H., Fox, N.C., Gamst, A., Holtzman, D.M., Jagust, W.J., Petersen, R.C., Snyder, P.J., Carrillo, M.C., Thies, B., Phelps, C.H., 2011. The diagnosis of mild cognitive impairment due to Alzheimer's disease: recommendations from the National Institute on Aging-Alzheimer's Association workgroups on diagnostic guidelines for Alzheimer's disease. Alzheimers Dement 7, 270–279. https://doi.org/10.1016/j.jalz.2011.03.008

Ashburner, J., 2007. A fast diffeomorphic image registration algorithm. NeuroImage 38, 95–113. https://doi.org/10.1016/j.neuroimage.2007.07.007

Ashburner, J., Friston, K.J., 2005. Unified segmentation. NeuroImage 26, 839–851. https://doi.org/10.1016/j.neuroimage.2005.02.018

Ayton, S., Faux, N.G., Bush, A.I., 2015. Ferritin levels in the cerebrospinal fluid predict Alzheimer's disease outcomes and are regulated by APOE. Nat Commun 6, 6760. https://doi.org/10.1038/ncomms7760

Azam, S., Haque, M.E., Balakrishnan, R., Kim, I.-S., Choi, D.-K., 2021. The Ageing Brain: Molecular and Cellular Basis of Neurodegeneration. Front Cell Dev Biol 9, 683459. https://doi.org/10.3389/fcell.2021.683459

Bahri, M.A., Plenevaux, A., Aerts, J., Bastin, C., Becker, G., Mercier, J., Valade, A., Buchanan, T., Mestdagh, N., Ledoux, D., Seret, A., Luxen, A., Salmon, E., 2017. Measuring brain synaptic vesicle protein 2A with positron emission tomography and [18F]UCB-H. Alzheimer's & Dementia: Translational Research & Clinical Interventions 3, 481–486. https://doi.org/10.1016/j.trci.2017.08.004

Bartzokis, G., 2011. Alzheimer's disease as homeostatic responses to age-related myelin breakdown. Neurobiology of Aging 32, 1341–1371. https://doi.org/10.1016/j.neurobiolaging.2009.08.007

Bartzokis, G., Lu, P.H., Mintz, J., 2007. Human brain myelination and amyloid beta deposition in Alzheimer's disease. Alzheimer's & Dementia 3, 122–125. https://doi.org/10.1016/j.jalz.2007.01.019

Bartzokis, G., Sultzer, D., Cummings, J., Holt, L.E., Hance, D.B., Henderson, V.W., Mintz, J., 2000. In Vivo Evaluation of Brain Iron in Alzheimer Disease Using Magnetic Resonance Imaging. Arch Gen Psychiatry 57, 47. https://doi.org/10.1001/archpsyc.57.1.47

Bastin, C., Bahri, M.A., Meyer, F., Manard, M., Delhaye, E., Plenevaux, A., Becker, G., Seret, A., Mella, C., Giacomelli, F., Degueldre, C., Balteau, E., Luxen, A., Salmon, E., 2020. In vivo imaging of synaptic loss in Alzheimer's disease with [18F]UCB-H positron emission tomography. Eur J Nucl Med Mol Imaging 47, 390–402. https://doi.org/10.1007/s00259-019-04461-x

Bulk, M., Abdelmoula, W.M., Nabuurs, R.J.A., van der Graaf, L.M., Mulders, C.W.H., Mulder, A.A., Jost, C.R., Koster, A.J., van Buchem, M.A., Natté, R., Dijkstra, J., van der Weerd, L., 2018. Postmortem MRI and histology demonstrate differential iron accumulation and cortical myelin organization in early- and late-onset Alzheimer's disease. Neurobiology of Aging 62, 231–242. https://doi.org/10.1016/j.neurobiolaging.2017.10.017

Calabrò, M., Rinaldi, C., Santoro, G., Crisafulli, C., Department of Biomedical and Dental Sciences and Morphofunctional Imaging, University of Messina, Italy, 2021. The biological pathways of Alzheimer disease: a review. AIMS Neuroscience 8, 86–132. https://doi.org/10.3934/Neuroscience.2021005

Callaghan, M.F., Freund, P., Draganski, B., Anderson, E., Cappelletti, M., Chowdhury, R., Diedrichsen, J., FitzGerald, T.H.B., Smittenaar, P., Helms, G., Lutti, A., Weiskopf, N., 2014. Widespread age-

medRxiv preprint doi: https://doi.org/10.1101/2023.04.14.23288516; this version posted April 17, 2023. The copyright holder for this preprint (which was not certified by peer review) is the author/funder, who has granted medRxiv a license to display the preprint in perpetuity. It is made available under a CC-BY-NC-ND 4.0 International license .

related differences in the human brain microstructure revealed by quantitative magnetic resonance imaging. Neurobiology of Aging 35, 1862–1872. https://doi.org/10.1016/j.neurobiolaging.2014.02.008

C.-C Tan, L.T., J.T. Yu, 2014. Biomarkers for preclinical Alzheimer's disease. J. Alzheimers Dis. JAD.

Chen, G., Adleman, N.E., Saad, Z.S., Leibenluft, E., Cox, R.W., 2014. Applications of multivariate modeling to neuroimaging group analysis: A comprehensive alternative to univariate general linear model. NeuroImage 99, 571–588. https://doi.org/10.1016/j.neuroimage.2014.06.027

Chen, J.-F., 2021. Enhancing myelin renewal reverses cognitive dysfunction in a murine model of Alzheimer's disease. Neuron.

Chen, M.-K., Mecca, A.P., Naganawa, M., Finnema, S.J., Toyonaga, T., Lin, S., Najafzadeh, S., Ropchan, J., Lu, Y., McDonald, J.W., Michalak, H.R., Nabulsi, N.B., Arnsten, A.F.T., Huang, Y., Carson, R.E., van Dyck, C.H., 2018. Assessing Synaptic Density in Alzheimer Disease With Synaptic Vesicle Glycoprotein 2A Positron Emission Tomographic Imaging. JAMA Neurol 75, 1215. https://doi.org/10.1001/jamaneurol.2018.1836

Dean, D.C., Hurley, S.A., Kecskemeti, S.R., O'Grady, J.P., Canda, C., Davenport-Sis, N.J., Carlsson, C.M., Zetterberg, H., Blennow, K., Asthana, S., Sager, M.A., Johnson, S.C., Alexander, A.L., Bendlin, B.B., 2017. Association of Amyloid Pathology With Myelin Alteration in Preclinical Alzheimer Disease. JAMA Neurol 74, 41–49. https://doi.org/10.1001/jamaneurol.2016.3232

DeKosky, S.T., Scheff, S.W., 1990. Synapse loss in frontal cortex biopsies in Alzheimer's disease: correlation with cognitive severity. Ann Neurol 27, 457–464. https://doi.org/10.1002/ana.410270502

Draganski, B., Ashburner, J., Hutton, C., Kherif, F., Frackowiak, R.S.J., Helms, G., Weiskopf, N., 2011. Regional specificity of MRI contrast parameter changes in normal ageing revealed by voxel-based quantification (VBQ). NeuroImage 55, 1423–1434. https://doi.org/10.1016/j.neuroimage.2011.01.052

Duijn, S.V., 2017. Cortical Iron Reflects Severity of Alzheimer's Disease. J. Alzheimers Dis.

Gonneaud, J., Chételat, G., 2018. Which is to blame for cognitive decline in ageing: amyloid deposition, neurodegeneration or both? Brain 141, 2237–2241. https://doi.org/10.1093/brain/awy174

Gorgolewski, K.J., Auer, T., Calhoun, V.D., Craddock, R.C., Das, S., Duff, E.P., Flandin, G., Ghosh, S.S., Glatard, T., Halchenko, Y.O., Handwerker, D.A., Hanke, M., Keator, D., Li, X., Michael, Z., Maumet, C., Nichols, B.N., Nichols, T.E., Pellman, J., Poline, J.-B., Rokem, A., Schaefer, G., Sochat, V., Triplett, W., Turner, J.A., Varoquaux, G., Poldrack, R.A., 2016. The brain imaging data structure, a format for organizing and describing outputs of neuroimaging experiments. Sci Data 3, 160044. https://doi.org/10.1038/sdata.2016.44

Gulisano, W., Maugeri, D., Baltrons, M.A., Fà, M., Amato, A., Palmeri, A., D'Adamio, L., Grassi, C., Devanand, D.P., Honig, L.S., Puzzo, D., Arancio, O., 2018. Role of Amyloid-β and Tau Proteins in Alzheimer's Disease: Confuting the Amyloid Cascade. JAD 64, S611–S631. https://doi.org/10.3233/JAD-179935

Gyger, L., Ramponi, C., Mall, J.F., Swierkosz-Lenart, K., Stoyanov, D., Lutti, A., von Gunten, A., Kherif, F., Draganski, B., 2021. Temporal trajectory of brain tissue property changes induced by electroconvulsive therapy. NeuroImage 232, 117895. https://doi.org/10.1016/j.neuroimage.2021.117895

Jack, C.R., Bennett, D.A., Blennow, K., Carrillo, M.C., Dunn, B., Haeberlein, S.B., Holtzman, D.M., Jagust, W., Jessen, F., Karlawish, J., Liu, E., Molinuevo, J.L., Montine, T., Phelps, C., Rankin, K.P., Rowe, C.C., Scheltens, P., Siemers, E., Snyder, H.M., Sperling, R., Contributors, Elliott, C., Masliah, E., Ryan, L., Silverberg, N., 2018. NIA□AA Research Framework: Toward a biological definition of Alzheimer's disease. Alzheimer's & Dementia 14, 535–562. https://doi.org/10.1016/j.jalz.2018.02.018

Jack, C.R., Knopman, D.S., Jagust, W.J., Petersen, R.C., Weiner, M.W., Aisen, P.S., Shaw, L.M., Vemuri, P., Wiste, H.J., Weigand, S.D., Lesnick, T.G., Pankratz, V.S., Donohue, M.C., Trojanowski, J.Q., 2013. Tracking pathophysiological processes in Alzheimer's disease: an

medRxiv preprint doi: https://doi.org/10.1101/2023.04.14.23288516; this version posted April 17, 2023. The copyright holder for this preprint (which was not certified by peer review) is the author/funder, who has granted medRxiv a license to display the preprint in perpetuity. It is made available under a CC-BY-NC-ND 4.0 International license .

updated hypothetical model of dynamic biomarkers. Lancet Neurol 12, 207–216. https://doi.org/10.1016/S1474-4422(12)70291-0

Jeremic, D., Jiménez-Díaz, L., Navarro-López, J.D., 2021. Past, present and future of therapeutic strategies against amyloid-β peptides in Alzheimer's disease: a systematic review. Ageing Res Rev 72, 101496. https://doi.org/10.1016/j.arr.2021.101496

Kalpouzos, G., Garzón, B., Sitnikov, R., Heiland, C., Salami, A., Persson, J., Bäckman, L., 2017. Higher Striatal Iron Concentration is Linked to Frontostriatal Underactivation and Poorer Memory in Normal Aging. Cerebral Cortex 27, 3427–3436. https://doi.org/10.1093/cercor/bhx045

Karakuzu, A., Appelhoff, S., Auer, T., Boudreau, M., Feingold, F., Khan, A.R., Lazari, A., Markiewicz, C., Mulder, M., Phillips, C., Salo, T., Stikov, N., Whitaker, K., de Hollander, G., 2022. qMRI-BIDS: An extension to the brain imaging data structure for quantitative magnetic resonance imaging data. Sci Data 9, 517. https://doi.org/10.1038/s41597-022-01571-4

Knudsen, G.M., Ganz, M., Appelhoff, S., Boellaard, R., Bormans, G., Carson, R.E., Catana, C., Doudet, D., Gee, A.D., Greve, D.N., Gunn, R.N., Halldin, C., Herscovitch, P., Huang, H., Keller, S.H., Lammertsma, A.A., Lanzenberger, R., Liow, J.-S., Lohith, T.G., Lubberink, M., Lyoo, C.H., Mann, J.J., Matheson, G.J., Nichols, T.E., Nørgaard, M., Ogden, T., Parsey, R., Pike, V.W., Price, J., Rizzo, G., Rosa-Neto, P., Schain, M., Scott, P.J., Searle, G., Slifstein, M., Suhara, T., Talbot, P.S., Thomas, A., Veronese, M., Wong, D.F., Yaqub, M., Zanderigo, F., Zoghbi, S., Innis, R.B., 2020. Guidelines for the content and format of PET brain data in publications and archives: A consensus paper. J Cereb Blood Flow Metab 40, 1576–1585. https://doi.org/10.1177/0271678X20905433

Lutti, A., Hutton, C., Finsterbusch, J., Helms, G., Weiskopf, N., 2010. Optimization and validation of methods for mapping of the radiofrequency transmit field at 3T. Magnetic Resonance in Medicine 64, 229–238. https://doi.org/10.1002/mrm.22421

M Mcfarquhar, S.W., S. Mckie, R. Emsley, J. Suckling, R. Elliott, 2016. Multivariate and repeated measures (MRM): A new toolbox for dependent and multimodal group-level neuroimaging data. NeuroImage.

McKhann, G.M., Knopman, D.S., Chertkow, H., Hyman, B.T., Jack, C.R., Kawas, C.H., Klunk, W.E., Koroshetz, W.J., Manly, J.J., Mayeux, R., Mohs, R.C., Morris, J.C., Rossor, M.N., Scheltens, P., Carrillo, M.C., Thies, B., Weintraub, S., Phelps, C.H., 2011. The diagnosis of dementia due to Alzheimer's disease: recommendations from the National Institute on Aging-Alzheimer's Association workgroups on diagnostic guidelines for Alzheimer's disease. Alzheimers Dement 7, 263–269. https://doi.org/10.1016/j.jalz.2011.03.005

Musiek, E.S., Holtzman, D.M., 2015. Three dimensions of the amyloid hypothesis: time, space and "wingmen." Nat Neurosci 18, 800–806. https://doi.org/10.1038/nn.4018

Nasrabady, S.E., Rizvi, B., Goldman, J.E., Brickman, A.M., 2018. White matter changes in Alzheimer's disease: a focus on myelin and oligodendrocytes. Acta Neuropathol Commun 6, 22. https://doi.org/10.1186/s40478-018-0515-3

Peng, Y., Chang, X., Lang, M., 2021. Iron Homeostasis Disorder and Alzheimer's Disease. Int J Mol Sci 22, 12442. https://doi.org/10.3390/ijms222212442

Peters, A., 2002. The effects of normal aging on myelin and nerve fibers: A review. Journal of Neurocytology 13.

Preibisch, C., Deichmann, R., 2009. Influence of RF spoiling on the stability and accuracy of T1 mapping based on spoiled FLASH with varying flip angles. Magnetic Resonance in Medicine 61, 125–135. https://doi.org/10.1002/mrm.21776

Salmon, E., Lekeu, F., Bastin, C., Garraux, G., Collette, F., 2008. Functional imaging of cognition in Alzheimer's disease using positron emission tomography. Neuropsychologia, Neuroimaging of Early Alzheimer's Disease 46, 1613–1623. https://doi.org/10.1016/j.neuropsychologia.2007.11.022

Scheff, S.W., Price, D.A., Schmitt, F.A., Mufson, E.J., 2006. Hippocampal synaptic loss in early Alzheimer's disease and mild cognitive impairment. Neurobiology of Aging 27, 1372–1384.

medRxiv preprint doi: https://doi.org/10.1101/2023.04.14.23288516; this version posted April 17, 2023. The copyright holder for this preprint (which was not certified by peer review) is the author/funder, who has granted medRxiv a license to display the preprint in perpetuity. It is made available under a CC-BY-NC-ND 4.0 International license .

https://doi.org/10.1016/j.neurobiolaging.2005.09.012

Spillantini, M.G., Goedert, M., 2013. Tau pathology and neurodegeneration. The Lancet Neurology 12, 609–622. https://doi.org/10.1016/S1474-4422(13)70090-5

Steiger, T.K., Weiskopf, N., Bunzeck, N., 2016. Iron Level and Myelin Content in the Ventral Striatum Predict Memory Performance in the Aging Brain. Journal of Neuroscience 36, 3552–3558. https://doi.org/10.1523/JNEUROSCI.3617-15.2016

Su, L., M. Blamire, A., Watson, R., He, J., Aribisala, B., T. O128;™Brien, J., 2016. Cortical and Subcortical Changes in Alzheimer's Disease: A Longitudinal and Quantitative MRI Study. Current Alzheimer Research 13, 534–544.

Tabachnick, B.G., Fidell, L.S., 2007. Using multivariate statistics, 5th ed. ed. Pearson/Allyn & Bacon, Boston.

Tabelow, K., 2019. "hMRI - A toolbox for quantitative MRI in neuroscience and clinical research. NeuroImage.

Tan, C.-C., Yu, J.-T., Tan, L., 2014. Biomarkers for preclinical Alzheimer's disease. J Alzheimers Dis 42, 1051–1069. https://doi.org/10.3233/JAD-140843

Terry, R.D., Masliah, E., Salmon, D.P., Butters, N., DeTeresa, R., Hill, R., Hansen, L.A., Katzman, R., 1991. Physical basis of cognitive alterations in alzheimer's disease: Synapse loss is the major correlate of cognitive impairment. Ann Neurol. 30, 572–580. https://doi.org/10.1002/ana.410300410

Thomas, B.A., Cuplov, V., Bousse, A., Mendes, A., Thielemans, K., Hutton, B.F., Erlandsson, K., 2016. PETPVC: a toolbox for performing partial volume correction techniques in positron emission tomography. Phys. Med. Biol. 61, 7975–7993. https://doi.org/10.1088/0031-9155/61/22/7975

Timmers, M., Tesseur, I., Bogert, J., Zetterberg, H., Blennow, K., Börjesson-Hanson, A., Baquero, M., Boada, M., Randolph, C., Tritsmans, L., Van Nueten, L., Engelborghs, S., Streffer, J.R., 2019. Relevance of the interplay between amyloid and tau for cognitive impairment in early Alzheimer's disease. Neurobiology of Aging 79, 131–141. https://doi.org/10.1016/j.neurobiolaging.2019.03.016

Timmler, S., Simons, M., 2019. Grey matter myelination. Glia 67, 2063–2070. https://doi.org/10.1002/glia.23614

van Bergen, J.M.G., Unschuld, P.G., Li, X., Hua, J., Schreiner, S.J., Steininger, S.C., F C Quevenco, M Wyss, A F Gietl, V Treyer, S E Leh, F Buck, R M Nitsch, K P Pruessmann, P C M Van Zijl, C Hock, 2016. Colocalization of cerebral iron with. Amyloid beta in Mild Cognitive Impairment. Sci. Rep.

Villemagne, V.L., Pike, K.E., Chételat, G., Ellis, K.A., Mulligan, R.S., Bourgeat, P., Ackermann, U., Jones, G., Szoeke, C., Salvado, O., Martins, R., O'Keefe, G., Mathis, C.A., Klunk, W.E., Ames, D., Masters, C.L., Rowe, C.C., 2011. Longitudinal assessment of Aβ and cognition in aging and Alzheimer disease. Annals of Neurology 69, 181–192. https://doi.org/10.1002/ana.22248

Wang, H.-T., Smallwood, J., Mourao-Miranda, J., Xia, C.H., Satterthwaite, T.D., Bassett, D.S., Bzdok, D., 2020. Finding the needle in a high-dimensional haystack: Canonical correlation analysis for neuroscientists. NeuroImage 216, 116745. https://doi.org/10.1016/j.neuroimage.2020.116745

Wang, S.-S., Zhang, Z., Zhu, T.-B., Chu, S.-F., He, W.-B., Chen, N.-H., 2018. Myelin injury in the central nervous system and Alzheimer's disease. Brain Research Bulletin 140, 162–168. https://doi.org/10.1016/j.brainresbull.2018.05.003

Weiskopf, N., Callaghan, M.F., Josephs, O., Lutti, A., Mohammadi, S., 2014. Estimating the apparent transverse relaxation time (R2*) from images with different contrasts (ESTATICS) reduces motion artifacts. Frontiers in Neuroscience 8.

Weiskopf, N., Suckling, J., Williams, G., Correia, M.M., Inkster, B., Tait, R., Ooi, C., Bullmore, E.T., Lutti, A., 2013. Quantitative multi-parameter mapping of R1, PD*, MT, and R2* at 3T: a multi-center validation. Front. Neurosci. 7. https://doi.org/10.3389/fnins.2013.00095

Yang, J., Pan, P., Song, W., Huang, R., Li, J., Chen, K., Gong, Q., Zhong, J., Shi, H., Shang, H., 2012. Voxelwise meta-analysis of gray matter anomalies in Alzheimer's disease and mild cognitive

medRxiv preprint doi: https://doi.org/10.1101/2023.04.14.23288516; this version posted April 17, 2023. The copyright holder for this preprint (which was not certified by peer review) is the author/funder, who has granted medRxiv a license to display the preprint in perpetuity. It is made available under a CC-BY-NC-ND 4.0 International license .

impairment using anatomic likelihood estimation. J Neurol Sci 316, 21–29. https://doi.org/10.1016/j.jns.2012.02.010

Yin, X., W Qian, Y Qiu, C Zhao, Z Zhou, J Bao, 2021. The Role of Amyloid-Beta and Tau in the Early Pathogenesis of Alzheimer's Disease. Med. Sci. Monit. Int. Med. J. Exp. Clin. Res.

Zecca, L., Youdim, M.B.H., Riederer, P., Connor, J.R., Crichton, R.R., 2004. Iron, brain ageing and neurodegenerative disorders. Nat Rev Neurosci 5, 863–873. https://doi.org/10.1038/nrn1537

Zeineh, M.M., Chen, Y., Kitzler, H.H., Hammond, R., Vogel, H., Rutt, B.K., 2015. Activated iron-containing microglia in the human hippocampus identified by magnetic resonance imaging in Alzheimer disease. Neurobiology of Aging 36, 2483–2500. https://doi.org/10.1016/j.neurobiolaging.2015.05.022

List of figures

Figure 1. Statistical parametric maps of the univariate analysis for AD and HC groups testing for the directional difference between the groups after adjusting for sex and age. 17
Figure 2. Distribution of voxel values within each MSPM significant cluster.. 18
Figure 3. Canonical vectors at the peak voxel of the significant clusters in the mGLM model. 19

List of tables

Table 1. Significant differences (FWER) between patients with Alzheimer's disease and healthy controls for MTsat and Vt maps.20
Table 2. Significant differences between AD and HC groups in the mGLM model**Error! Bookmark not defined.**

medRxiv preprint doi: https://doi.org/10.1101/2023.04.14.23288516; this version posted April 17, 2023. The copyright holder for this preprint (which was not certified by peer review) is the author/funder, who has granted medRxiv a license to display the preprint in perpetuity. It is made available under a CC-BY-NC-ND 4.0 International license .

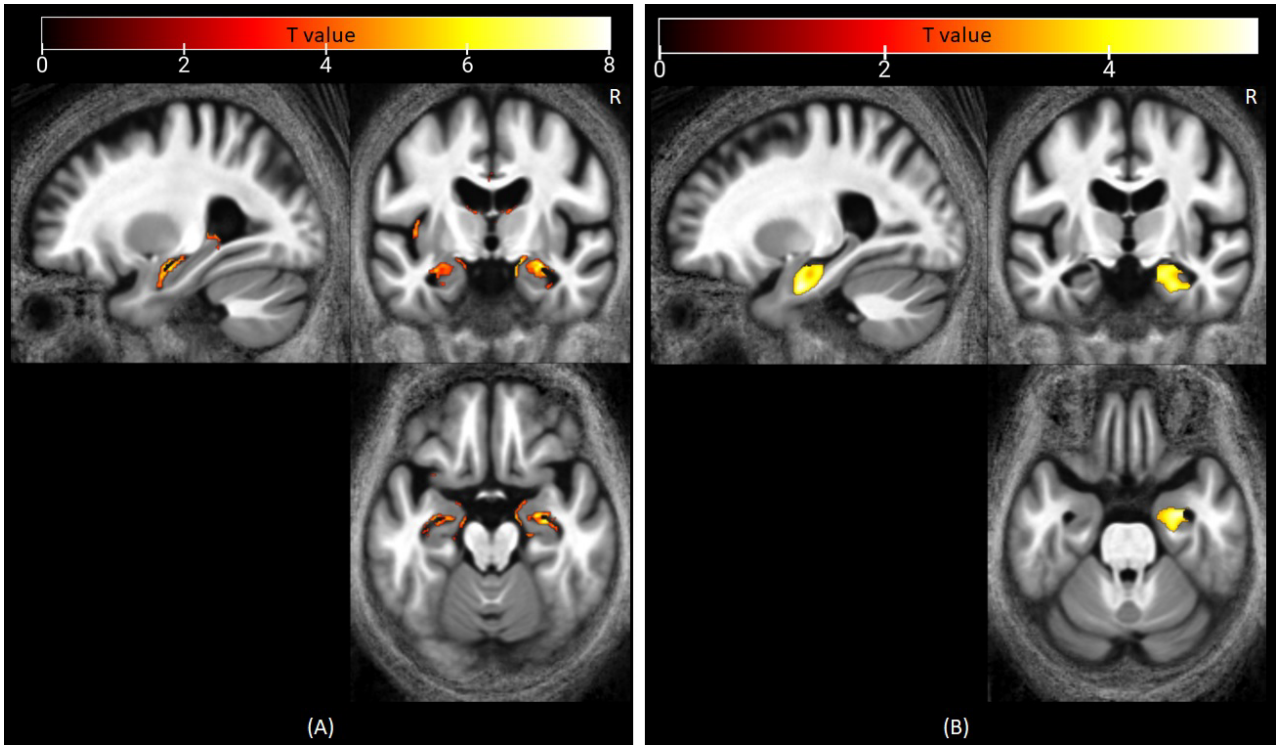

Figure 1. Statistical parametric maps of the univariate analysis for AD and HC groups testing for the directional difference between the groups after adjusting for sex and age. The results are overlaid on the average MTsat image and are displayed at $p < .05$ corrected at cluster-level. A) The results testing for $Vt_{AD}<Vt_{HC}$ specify lower values in the AD patients bilaterally in the hippocampus as well as the thalamus, middle cingulate gyrus, and left posterior and anterior insula. B) The results testing for $MTsat_{AD}<MTsat_{HC}$ show smaller intensities in the right hippocampus of the AD group.

medRxiv preprint doi: https://doi.org/10.1101/2023.04.14.23288516; this version posted April 17, 2023. The copyright holder for this preprint **(which was not certified by peer review)** is the author/funder, who has granted medRxiv a license to display the preprint in perpetuity. It is made available under a CC-BY-NC-ND 4.0 International license .

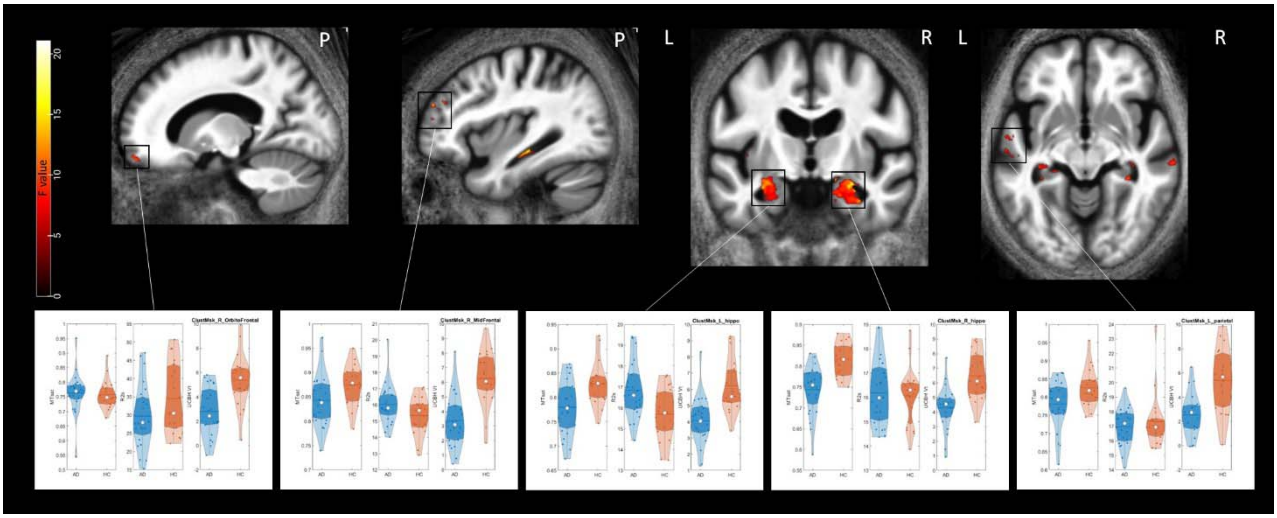

Figure 2. Distribution of voxel values within each MSPM significant cluster. Each violin plot represents the distribution, across the subjects in their group (AD in blue and HC in red), of mean values in the original quantitative map within each cluster, after adjusting for sex and age. White circles represent the median value within each group per cluster. The range of y axes is based on the variations within each modality. The first and third quartiles are shown with darker shadows within each violin. The mean value within each group per modality and cluster is shown with the horizontal line.

medRxiv preprint doi: https://doi.org/10.1101/2023.04.14.23288516; this version posted April 17, 2023. The copyright holder for this preprint **(which was not certified by peer review)** is the author/funder, who has granted medRxiv a license to display the preprint in perpetuity. It is made available under a CC-BY-NC-ND 4.0 International license .

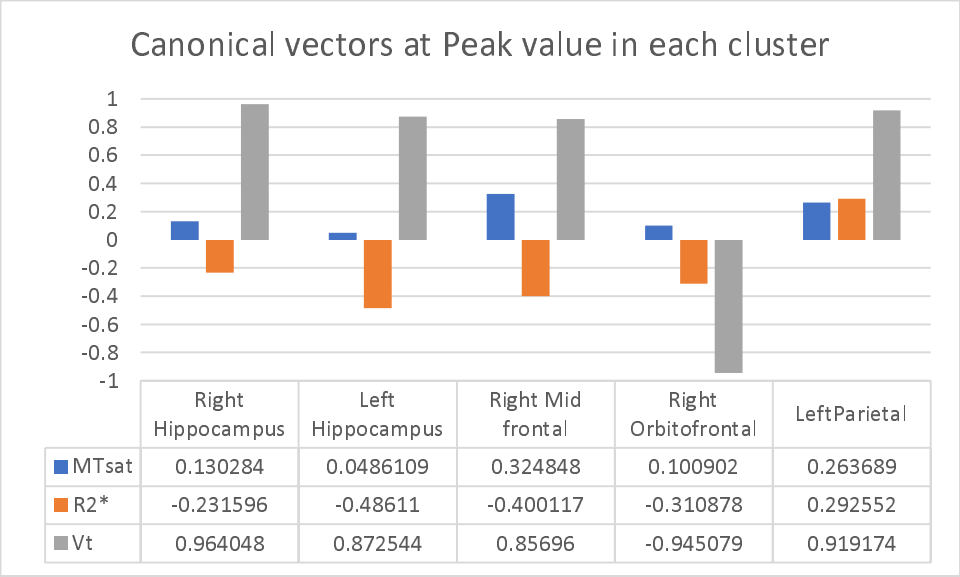

Figure 3. Canonical vectors at the peak voxel of the significant clusters in the mGLM model.

medRxiv preprint doi: https://doi.org/10.1101/2023.04.14.23288516; this version posted April 17, 2023. The copyright holder for this preprint (which was not certified by peer review) is the author/funder, who has granted medRxiv a license to display the preprint in perpetuity. It is made available under a CC-BY-NC-ND 4.0 International license .

Table 1. Significant differences between patients with Alzheimer's disease and healthy controls for MTsat and Vt maps. Brain regions were labeled with the aal3 atlas toolbox in SPM. This table shows up to 2 peaks (at least 8mm apart) within each cluster. Coordinates are MNI coordinates.

Peak [x y z] coordinates	Cluster P-value (FWER)	Cluster size	Brain region
MTsat (df=39)			
[31 –7 –27]	.001	2508	Right Hippocampus
[24 -7 -21]			Right Amygdala
Vt (df=39)			
[25 –10 -14]	.000	1983	Right Hippocampus
[26 -9 –18]			Right Amygdala
[-29 –14 –15]	.000	2219	Left Hippocampus
[-14 -21 17]			Left Thalamus
[3 -6 9]	.000	229	Right Thalamus
[-42 -7 2]	.000	303	Left Posterior Insula
[0 –18 33]	.001	217	Middle Cingulate Gyrus
[-38 15 –12]	.001	201	Left Anterior Insula

medRxiv preprint doi: https://doi.org/10.1101/2023.04.14.23288516; this version posted April 17, 2023. The copyright holder for this preprint (which was not certified by peer review) is the author/funder, who has granted medRxiv a license to display the preprint in perpetuity. It is made available under a CC-BY-NC-ND 4.0 International license .

Table 2. Significant differences between AD and HC groups in the mGLM model. Brain regions were labeled with the aal3 atlas toolbox in SPM. This table shows up to 2 peaks (at least 8mm apart) within each cluster.

MSPM (df=37)			
Peak [x y z] coordinates	Cluster P-value (FWER)	Cluster size	Brain region
[25 -10 -14]	.000	1772	Right Hippocampus
[30 -7 -22]			Right Amygdala
[-27 -12 -15]	.021	895	Left Hippocampus
[-30 -8 -23]			Left Amygdala
[40 49 22]	.028	115	Right Middle Frontal
[-62 -44 35]	.045	19	Left Inferior Parietal
[8 34 -27]	.047	13	Right Orbitofrontal